Channel optimization of high-intensity laser beams in millimeter-scale plasmas

L. Ceurvorst,[1,*] A. Savin,[1] N. Ratan,[1] M. F. Kasim,[1] J. Sadler,[1] P. A. Norreys,[1,2] H. Habara,[3] K. A. Tanaka,[3,4] S. Zhang,[5] M. S. Wei,[6] S. Ivancic,[7] D. H. Froula,[8] and W. Theobald[7]

[1]*Clarendon Laboratory, Department of Physics, University of Oxford, Parks Road, Oxford, OX1 3PU United Kingdom*
[2]*STFC Rutherford Appleton Laboratory, Chilton, Didcot, OX11 0QX United Kingdom*
[3]*Graduate School of Engineering, Osaka University, Suita, Osaka 5650871, Japan*
[4]*ELI-NP/IFIN-HH, 30 Reactorului Street, Magurele, Ilfov County, P. O. Box MG-6, 077125 Romania*
[5]*Department of Mechanical and Aerospace Engineering, University of California at San Diego, La Jolla, California 92093, USA*
[6]*General Atomics, San Diego, California 92121, USA*
[7]*Laboratory for Laser Energetics, University of Rochester, Rochester, New York 14623, USA*
[8]*Department of Physics and Astronomy, University of Rochester, Rochester, New York 14623, USA*

(Received 3 February 2017; revised manuscript received 26 February 2018; published 20 April 2018)

Channeling experiments were performed at the OMEGA EP facility using relativistic intensity ($>10^{18}$ W/cm^2) kilojoule laser pulses through large density scale length ($\sim$390–570 μm) laser-produced plasmas, demonstrating the effects of the pulse's focal location and intensity as well as the plasma's temperature on the resulting channel formation. The results show deeper channeling when focused into hot plasmas and at lower densities, as expected. However, contrary to previous large-scale particle-in-cell studies, the results also indicate deeper penetration by short (10 ps), intense pulses compared to their longer-duration equivalents. This new observation has many implications for future laser-plasma research in the relativistic regime.

DOI: 10.1103/PhysRevE.97.043208

I. INTRODUCTION

The propagation of a laser beam through an underdense plasma is of fundamental interest in plasma physics research. Above a power threshold of $P_{\rm cr} \approx 17(n_c/n_e)$ GW, where n_c is the critical density and n_e the electron density, the laser beam will self-focus due to relativistic mass increases, effectively creating a self-induced waveguide from which it is able to evacuate the electrons [1–4]. This in turn causes the ions to be expelled due to charge separation, resulting in the formation of a persistent low-density channel [5–7]. This channeling process is useful in a wide variety of applications in current-day physics research, including ion beam generation via radiation pressure acceleration [8–14], electron injection in plasma wakefield accelerators [15–18], betatron emissions [19,20], and fast ignition inertial confinement fusion [21–24].

All of these applications require control of the channeling beam's propagation. However, several instabilities occur during the pulse's travel time which may erode the quality of the resulting channel. Perhaps most notable are the filamentation [25–29] and hosing instabilities [30–32] which together cause the pulse to bifurcate and alter its propagation direction. By doing so, the electromagnetic energy in any given beamlet is reduced and the resulting fast particles or photons in these schemes will be misdirected. It is therefore imperative to determine the ideal framework for controlling and thereby maximizing the quality of the resulting channel.

To address these issues, a channeling experiment was performed at the OMEGA EP facility focused on establishing the optimum parameters for channeling in large-scale length plasmas. Several factors had to be taken into account in choosing which parameters to explore. For instance, if a fast ignition experiment were to have a long coast phase, that is, a long time between the end of the drive pulses and stagnation, then the plasma would cool significantly. However, this cooling would cause thermal filamentation to increase due to an increase in collisionality within the plasma [26]. Further, waiting gives the plasma more time to expand, creating a larger density scale length which could affect propagation. Thus the relative timing of the drive beam and the channeling beam was chosen to be the first parameter to be scanned.

Further, the whole-beam self-focusing (superpenetration) approach to channeling presents a method of achieving deeper channeling through relativistic transparency while minimizing filamentation [33,34]. To do so, the laser pulse must be focused at low densities in order to allow relativistic self-focusing to reduce the spot size before the pulse reaches the quarter-critical density isosurface [35]. While the original papers on this process did contain experimental results and show great promise, those experiments were performed with a much smaller scale length than is obtainable at the OMEGA EP facility. Thus, in order to test the feasibility of the scheme on large-scale length plasmas, this experiment's second varied parameter was the focal position of pulses.

Finally, while higher intensity pulses theoretically would be able to penetrate deeper into a plasma due to relativistically induced transparency [36], previous numerical work has illustrated that this is not an energy efficient process as excessive levels of kinetic energy are transferred to the electron species [37]. Thus the intensity of pulses with similar total energies

*Present address: Université de Bordeaux-CNRS-CEA, Centre Lasers Intenses et Applications, UMR 5107, 33405 Talence, France; luke.ceurvorst@u-bordeaux.fr

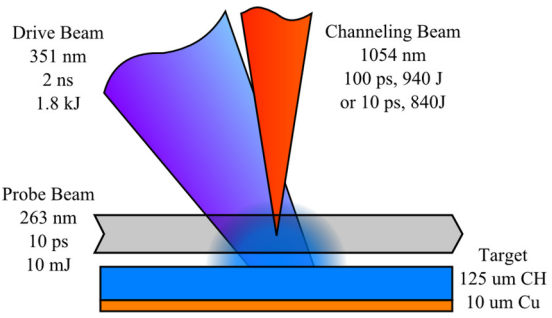

FIG. 1. Schematic of experimental setup. A 3ω drive beam ablates the surface of a plastic target, generating a plasma plume. On completion of the driving phase, a 1ω channeling pulse begins propagation through the plasma normal to the target's surface. A 4ω probe pulse is used to observe the resulting channel formations.

needed to be explored and became the third and final parameter to be varied in this experiment.

II. EXPERIMENTAL DESIGN

The experiment design was as follows and is illustrated in Fig. 1. An ultraviolet (UV) square pulse drive beam of 1.8 kJ energy and 2 ns duration with wavelength $\lambda_{UV} = 351$ nm irradiated a copper-backed polystyrene target. The CH layer was 125 μm thick with 10 μm Cu backing for use as a diagnostic for hot electron generation via Cu K_α imaging. On completion of the drive pulse, a channeling beam was targeted at the resulting plasma plume along its density gradient using an $f/2$ off-axis parabola. This infrared (IR), $\lambda_{IR} = 1.054\,\mu$m, pulse had a Gaussian longitudinal profile and alternated energy and duration between approximately 940 J over 100 ps and 840 J over 10 ps. The vacuum focal spots for these shots were inferred and on average contained 80% of the laser energy in an 18 μm radius for the 100-ps shots and a 15 μm radius for the 10-ps shots. These equate to averaged intensities and corresponding dimensionless vector potentials of approximately 9.0×10^{17} W cm^{-2} ($a_0 \approx 0.85$) and 1.2×10^{19} W cm^{-2}($a_0 \approx 3.1$), respectively. Thus the 100-ps pulse will be referred to as the low-intensity beam and the 10-ps pulse the high-intensity beam. Finally, the resulting channels were diagnosed primarily through the use of a 10-ps, 10-mJ, 4ω probe beam ($\lambda_{probe} = 263$ nm) passing transversely through the channeling beam's propagation axis. The polarization of the beams was determined by their compressors. As a result, the 10-ps beams were s-polarized and the 100-ps beams were p-polarised relative to the transverse probe.

Fixing time $t_0 = 0$ ps, the shot timings were as follows: The UV drive pulse began interacting with the target at either time $t_{hot} = -2.0$ ns, herein known as the 'hot' shots, or at time $t_{cold} = -3.5$ ns, the "cold" shots. The low-intensity pulse was injected into the plasma so that its peak was delivered at $t_{low} = 0$ ps while the high-intensity pulse's peak was injected at time $t_{high} = 40$ ps. This was done so that both pulses would complete their propagation at approximately the same time. The probe peak timing was set to $t_{probe} = 60$ ps in order to align with the end of each channeling pulse's propagation.

Simulations were performed using the radiation-hydrodynamics code FLASH to give the predicted density and temperature profiles used to identify the focal positions of the IR pulse. The results of these simulations are shown for both the hot and cold scenarios in Fig. 2, where $Z = 0$ is fixed at the original target surface. As can be seen, the temperature profile shows significant cooling of the plasma between the hot and cold plasmas, with the hot plasmas around 650 eV in the low-density regions, peaking at 1.3 keV near the ablation front while the cold plasmas remain a near constant 185 eV throughout the interaction region. At the same time, the density profile's scale length increases from $375 \pm 8\,\mu$m in the hot simulation to $612 \pm 6\,\mu$m in the cold simulation. Based on this, the focal position of the hot beam was varied among $Z = 1500\,\mu$m, 900 μm, and 300 μm, corresponding to predicted density values at focus of approximately 0.08 n_c, 0.25 n_c, and 1.5 n_c, where $n_c = 1.0 \times 10^{21}$ cm^{-3} refers to the critical density for the IR pulse. In the cold plasma, the pulses were focused at about $Z = 1700\,\mu$m, corresponding to a density of 0.08 n_c.

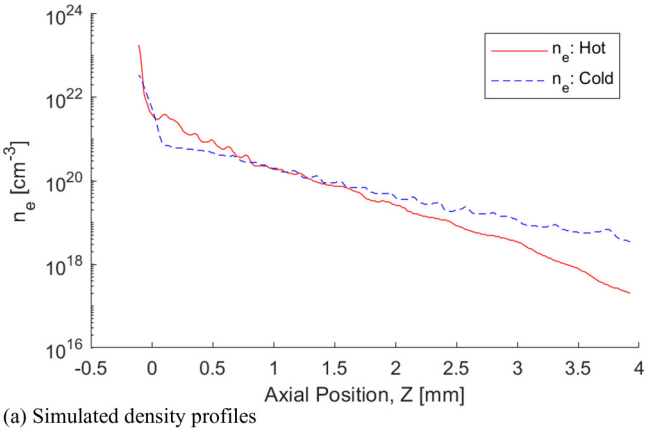

(a) Simulated density profiles

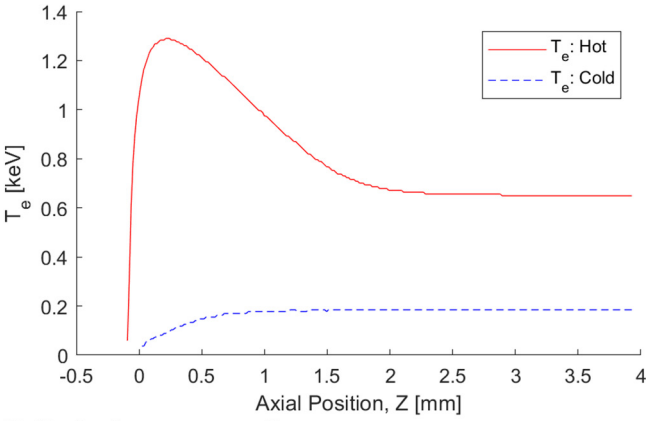

(b) Simulated temperature profiles

FIG. 2. FLASH simulations for the channeling parameters experiment. As can be seen from these simulations, the expected density profile is expected to expand to a larger scale length 1.5 ns after the end of the drive pulse ("Cold" simulations) compared to 0 ns delay ("Hot" simulations). The electron temperature dramatically cools during this period as well.

As stated above, the primary diagnostic used to observe the interaction of the channeling pulse with the plasma was the 4ω probe beam which passed transversely through the channel and was collected by several diagnostics including

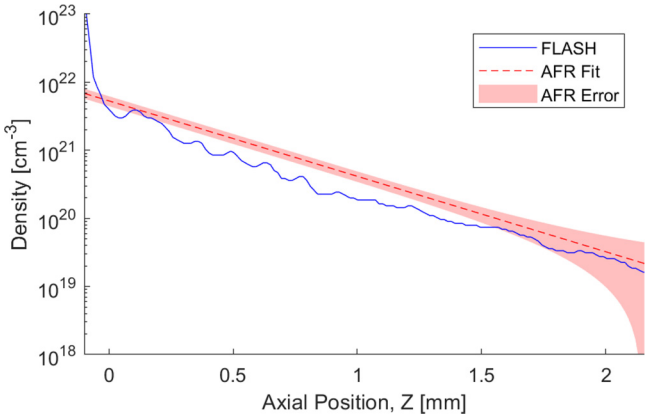

FIG. 3. AFR density reconstruction for the channeling parameters experiment. Shown is a sample reconstructed density profile from a hot plasma in comparison to the corresponding FLASH simulations. While the scale lengths were comparable, the FLASH simulations were approximately half to a third of the AFR reconstruction for much of the interaction region.

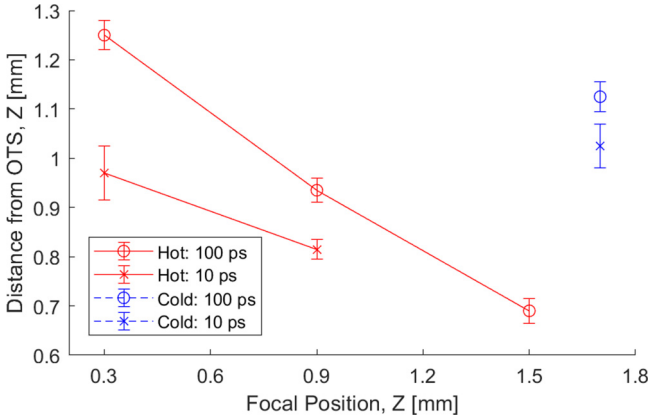

FIG. 4. Channel penetration. The final distances from the original target surface (OTS) are plotted against the vacuum focal position for the 100 ps and 10 ps in both the hot and cold plasmas. Deeper penetration would therefore have a lower value. These measurements were made using the 4ω probe.

Faraday rotation polarimetry, shadowgraphy, and angular filter refractometry (AFR). These were then used to reconstruct the density profile of the plasma as well as observe both the channel depth and the filamentation of the channeling pulse. A von Hamos spectrometer was in place as a secondary diagnostic to measure the fast electron generation.

III. DENSITY RECONSTRUCTION

In order to confirm the accuracy of the FLASH simulations used in designing the experiment, the density profiles were measured using the AFR diagnostic [38]. This method of measuring plasma density profiles is able to produce consistent quantitative measurements in near-critical plasmas by applying contour lines for fixed refraction angles to a probe beam. These lines then allow the user to spatially determine the phase of the probe and, by doing so, determine the overall density profile. The total error in this reconstruction is approximately $\pm 15\%$. However, this error increases at low densities due to the insensitivity of the diagnostic to global density shifts. This results in an absolute error greater than the lowest density measured.

Each reconstructed profile was well fitted with a single exponential function with the coefficient of determination for these fits given as $R^2 \geqslant 0.994$. The average profile had a $392 \pm 6\,\mu$m scale length for the hot plasmas and $570 \pm 20\,\mu$m for the cold plasmas. An example fit in a hot plasma is plotted against the corresponding FLASH density profile in Fig. 3. As can be seen, the reconstruction deviates slightly from the simulations, resulting in the pulses being focused instead at approximately $0.12 \pm 0.03\ n_c$, $0.53 \pm 0.08\ n_c$, and $2.5 \pm 0.4\ n_c$ in the hot plasma and at $0.11 \pm 0.03\ n_c$ in the cold plasma. While these do differ from the originally intended density values, the low-density focal position is still significantly below the quarter-critical surface, while the mid- and high-density points are still focused at underdense and overdense points in the plasma. Thus they are still sufficient for the purposes of this experiment.

IV. CHANNEL DEPTHS

The penetration depth for each pulse was determined by calculating the distance between the original target surface and the nearest point of bulk perturbation shown in the AFR images. The target's initial location was established from reference shots. Note that the AFR's data was used instead of the shadowgraphy results because several of the high-intensity shots produced a large enough electromagnetic pulse to disable the shadowgraphy camera. However, as will be seen shortly, the features in each diagnostic extend to the same depth, and so the AFR was deemed an appropriate tool to determine these depths.

The depth calculation does not include the filament-like structures seen in front of the channels which will be discussed in more detail in Sec. VIII. Figure 4 illustrates the results of this calculation for various applicable shots. The resolution of the AFR diagnostic was approximately $1.9\,\mu$m. However, uncertainty in the original target location and the clarity of the features being analyzed introduced additional error. Note that there is no data for the lowest focal density 10-ps shot in a hot plasma as the probe pulse was delivered 5 ps before the channeling pulse due to jitter in the timings, thereby missing the full channel development. Several interesting trends can be taken from this data.

V. TIMING DEPENDENCE

Due to the limited number of shots in this experiment, there were only two cold plasma shots (one high-intensity, one low-intensity), both focused 1.7 mm away from the original target surface at a density of $0.11 \pm 0.03\ n_c$. The comparable hot plasma shots were focused at $Z = 1.5$ mm with a corresponding density of $0.12 \pm 0.03\ n_c$. The AFR and shadowgraphy results are displayed in Fig. 5.

Both shadowgraphs and AFR images were cropped and displayed here to illustrate the fact that both diagnostics show the same channel depth, thereby justifying the Sec. IV's measurements. Horizontal red lines are superimposed onto these images at the depths measured in Fig. 4.

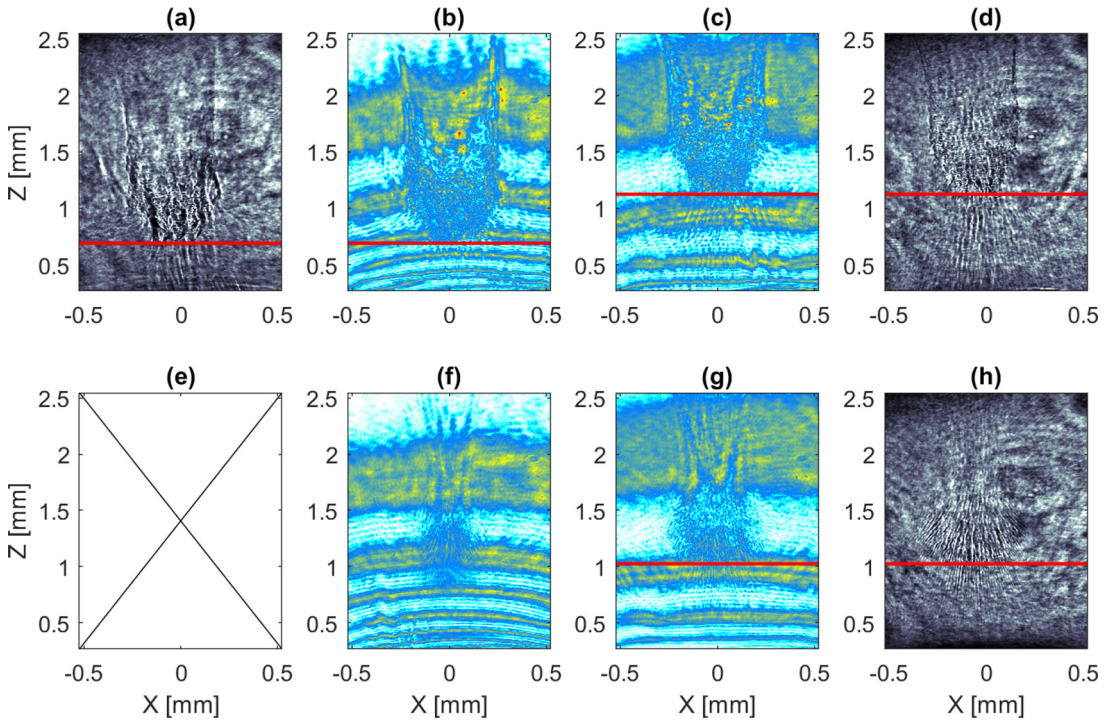

FIG. 5. AFR and shadowgraphy images for the channel depth timing dependence. Shadowgraphs are shown in the outer columns and AFR images are shown in the inner columns, each having been cropped to show the region of interest. The top row shows the results of the 100-ps beam in a hot plasma [(a) and (b)] compared to a cold plasma [(c) and (d)]. The bottom row does the same for the 10-ps beam with (f) showing the results of the hot plasma shot and (g) and (h) showing the cold plasma shot. Note that (e) is empty due to EMP disabling the shadowgraphy camera for this shot. The horizontal red lines are superimposed at the measured channel depth as plotted in Fig. 4. No superimposed line is present in (f) as the probe arrived prior to the channeling beam, meaning that the observed channel here is incomplete.

Filamentation qualitatively appears to be worse in Fig. 5(a) than Fig. 5(d), which could initially suggest increased filamentation in a hot plasma counter to what was previously argued. However, using the AFR density reconstruction, the cold plasma shot only reached $0.30 \pm 0.05\ n_c$, just past the quarter-critical isosurface where filamentation has the greatest growth rate [34]. Thus, it is to be expected that less filamentation would be present in this case, and these results do not speak to the relationship between plasma temperature and filamentation.

While it is difficult to measure filamentation from these images, channel depth may readily be obtained. As can be seen, the channels clearly reached a greater depth when no delay was present between the drive and channeling beams. Even in the case of Fig. 5(f) where only approximately half of the channel development is captured, the hot plasma shot had already passed the depth achieved in a cold plasma as shown in Figs. 5(g) and 5(h).

This increased depth in the hot plasmas more likely has to do with the density profile rather than the temperature of the plasma. For the bulk of the interaction region, the density will be greater in the cold plasmas as the high pressure near the ablation front will have caused the high density region to expand outwards. The FLASH simulations predict that this will be true for $Z \gtrsim 1$ mm as can be seen in Fig. 2(a), though the AFR fits suggest that this may be closer to $Z \gtrsim 0.11$ mm which would then cover the entire interaction region. In a significantly underdense plasma, the channel depth is determined by the number of particles with which the beam has interacted [32]. Because the density is greater in the cold plasma, it is appropriate that the channel would not have penetrated as deeply.

VI. FOCAL POSITION DEPENDENCE

The strong downward slope in Fig. 4 illustrates that the pulses were clearly able to penetrate deeper into the plasma when they were focused further from the target surface. This lends support to the whole-beam self-focusing scheme referenced in the introduction. The pulses focused at a high density had a larger spot size as they propagated through the plasma, and thus they were more susceptible to filamentation [34] while interacting with more particles, leading to earlier pulse depletion [32].

This deterioration of the channel's quality may be seen clearly by looking at the shadowgraphs and AFR results of the low-intensity channeling beam at various focal positions in hot plasmas as shown in Figs. 6(a)–6(c). It is worth noting that even though relativistic self-focusing is expected to have occurred, the channels themselves are quite wide. This may be attributed in part to filamentation. The shadowgraph of the low focal density pulse in Fig. 6(a) illustrates this well with the fingerlike structures seen near the head of the channel. Each of these filaments appears to be 10–25 μm in diameter as a rough approximation, though an exact measurement is impossible with the present diagnostics. Tomographical probing could be a viable method for gaining a more complete picture of the channel's structure. It is worth noting that these filaments

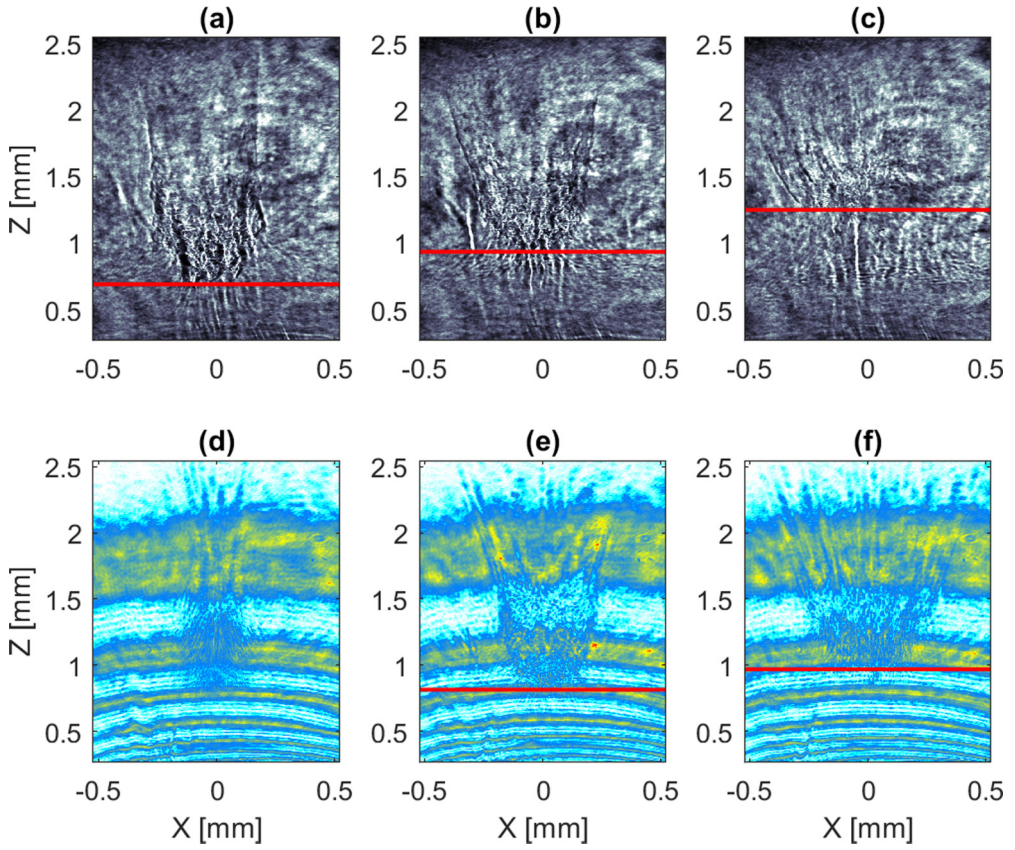

FIG. 6. AFR and shadowgraphy images for the channel depth focal position dependence. Shadowgraphs for the 100-ps pulse in hot plasmas are shown for focal positions (a) 1.5 mm, (b) 0.9 mm, and (c) 0.3 mm. Due to issues with the shadowgraphy camera on the high-power shots, AFR images are shown instead for the 10-ps pulse at focal positions (d) 1.5 mm, (e) 0.9 mm, and (f) 0.3 mm. Superimposed horizontal red lines indicate the measured channel depth. Note that (a) and (d) are reproduced from Figs. 5(a) and 5(f), respectively, for ease of viewing.

appear more strongly at the head of the channel than earlier in its formation. This is due to the pulse continuing to erode the walls between the pulses as seen previously in particle-in-cell (PIC) simulations [37] and experiments [39].

These filaments would be seemingly at odds with the predictions of the whole-beam self-focusing scheme. However, there are a number of explanations for why the pulse continued to filament. First, the pulse was not focused at a low-enough density. According to the scheme, the pulse would have to be focused to a point which would allow self-focusing to shrink the spot size to approximately the plasma wavelength by the time it reached the quarter-critical isosurface. If there was insufficient self-focusing, this would not be obtained. Additionally, whole-beam self-focusing assumes an ideal laser pulse with a smooth transverse profile while realistic pulses are often speckled. This means that realistic pulses have severe intensity modulations and are not perfectly shaped into the desired profile transversely due to deformations of the phase front. Figure 7 shows an example spot profile of the channeling beam used in this experiment when focused in vacuum—in this case, the 100-ps beam to be focused at $Z = 1.5$ mm in the hot plasma. As can be seen, strong speckling is present with several peaks separated by a few microns.

Speckling affects the pulse's ability to focus in vacuum, altering the Rayleigh length away from the theoretical value of $\pi w_0^2/\lambda$ which assumes a perfect Gaussian beam. An imperfect pulse focused off of an $f/2$ parabola to an 18-μm spot size at the OMEGA EP facility has previously been experimentally measured to have a Rayleigh length of approximately $90 \pm 30\,\mu$m before focus and $110 \pm 20\,\mu$m after focus [40]. This is several multiples less than the variation in the focal positions, indicating that these variations were more than sufficient to cause significantly different beam profiles at any point within the plasma. Additionally, these intensity modulations will alter the pulse's interaction with the plasma, especially by causing ponderomotive filamentation.

In order to test this effect, PIC simulations were run using OSIRIS, a two-dimensional (2D), fully relativistic, massively parallel particle-in-cell code [41], on the ARCHER UK National Supercomputing Services [42]. A p-polarised 10-ps pulse (0.5-ps rise and fall times and 9.5-ps flat time) was focused 392 μm into an inhomogeneous deuterium plasma with a 392-μm scale length in a 784 μm $\times$ 150 μm window. This pulse's profile was either a perfect Gaussian pulse with 80% of its energy contained within a 15-μm radius and $a_0 = 3.1$, herein known as the "perfect beam," or a combination of five Gaussian beams fitted to a previously obtained OMEGA pulse profile of comparable total energy, the "imperfect" beam. The fit of this imperfect beam is shown in Fig. 8. This profile was chosen rather than one present in this experiment as it lent itself well to a single line out. Note that the data shown here are fluent, which is proportional to a_0^2. The

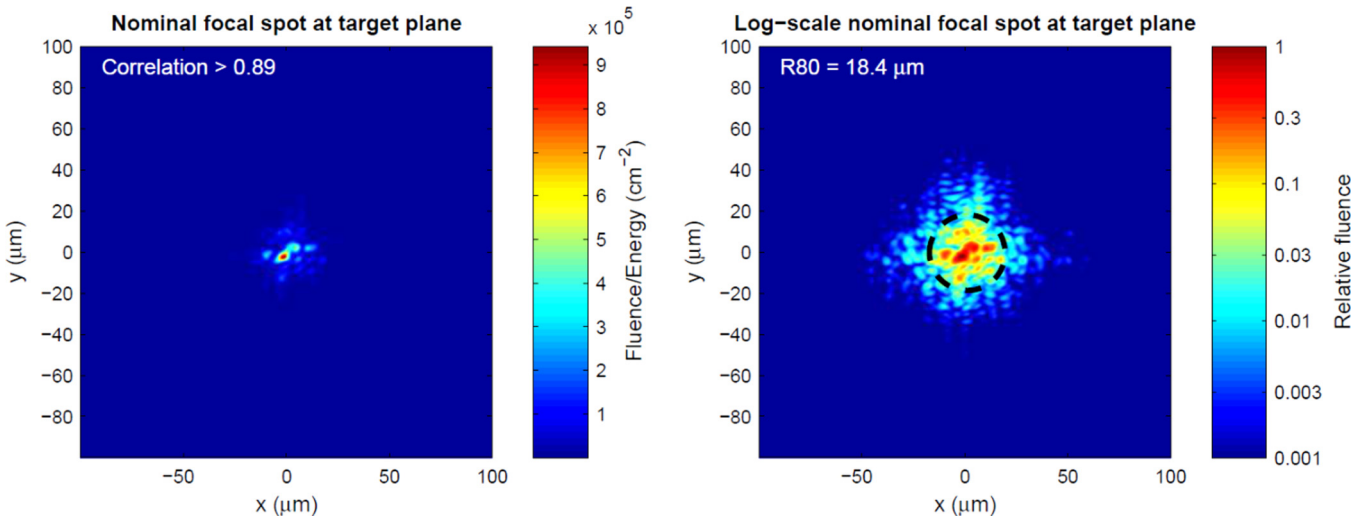

FIG. 7. Channeling beam profile. Strong speckling of the channeling beam at focus may be observed. The right image shows the nominal fluence on a log-scale with 80% of the energy contained within an 18.4-μm radius as indicated by the black dotted line.

intensity of this pulse was scaled so that it possessed the same total energy as the perfect beam. The plasma was made up of three fluids: electrons, fully ionized carbon ions, and hydrogen ions. The density at the center of the window was 0.11 n_c, and the grid size was 15 680 × 3000 for a 50-nm resolution.

To ensure that the beam had been correctly simulated, the plasma was first omitted from the simulation to test the pulse profile in vacuum. Unfortunately, as shown in Fig. 9, the fitted beam was not successfully recreated. This could have to do with the relative phase of individual speckles. As can be seen, the pulse only had two peaks at focus which were much broader than originally intended. Still, the pulse is not perfect and can give some indication of the effects of speckling, though this simulation will instead represent the minimal effects rather than the realistic intended results of speckling.

The results of the full simulations are shown in Fig. 10. As expected, the imperfect beam simulation did experience more filamentation early in its propagation than the perfect beam, diverging into two primary filaments in line with the intensity distribution. However, after 3 ps, much of the ponderomotively formed density perturbation had been eroded and the pulse was able to continue propagation mostly as a single beam. This was consistent with simulations which were performed in preparation for the experiment which utilized a much more sharply speckled beam. Meanwhile, the perfect beam simulation still did experience low-level filamentation after undergoing self-focusing. This occurred through the intensity modulations induced by deconstructive interference during

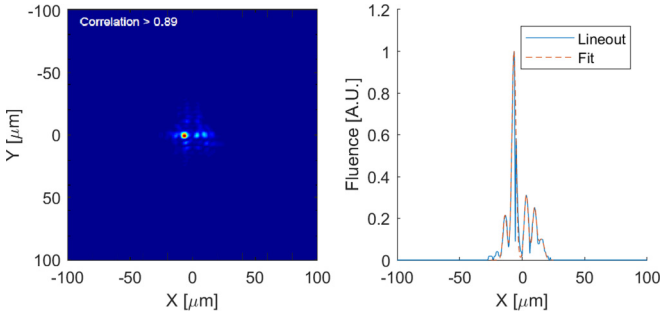

FIG. 8. Simulated channeling beam profile. The left image shows the nominal fluence of the focal spot at the target plane. A horizontal lineout was taken at $Y = 0\,\mu$m and fitted with five Gaussian functions. The results of this lineout and fit are shown in the bottom plot.

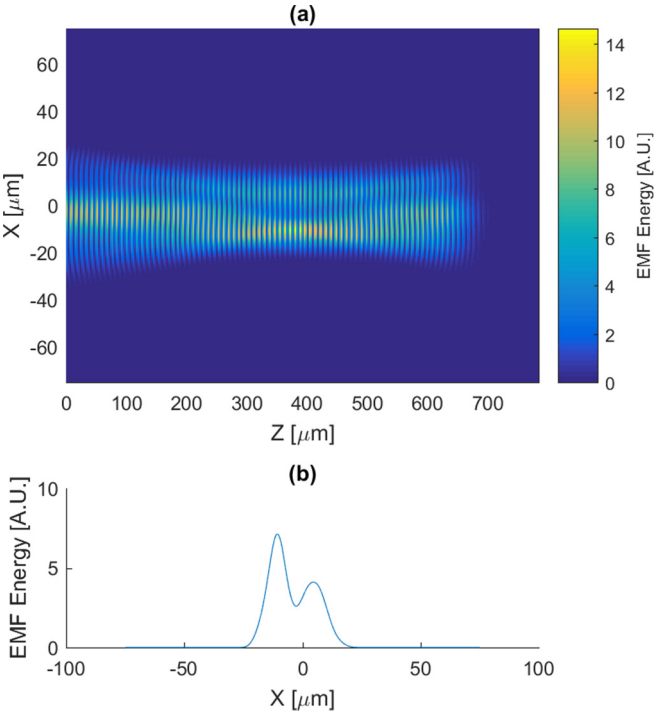

FIG. 9. Simulated intensity profile of imperfect beam in vacuum. (a) The spatially resolved electromagnetic energy of the vacuum simulation is shown after 2.5 ps in (a). A lineout at $Z = 392\,\mu$m was taken and is plotted in (b). As can be seen, the simulation did not successfully capture the fitted spot shown in Fig. 8, but instead generated two broad peaks at focus.

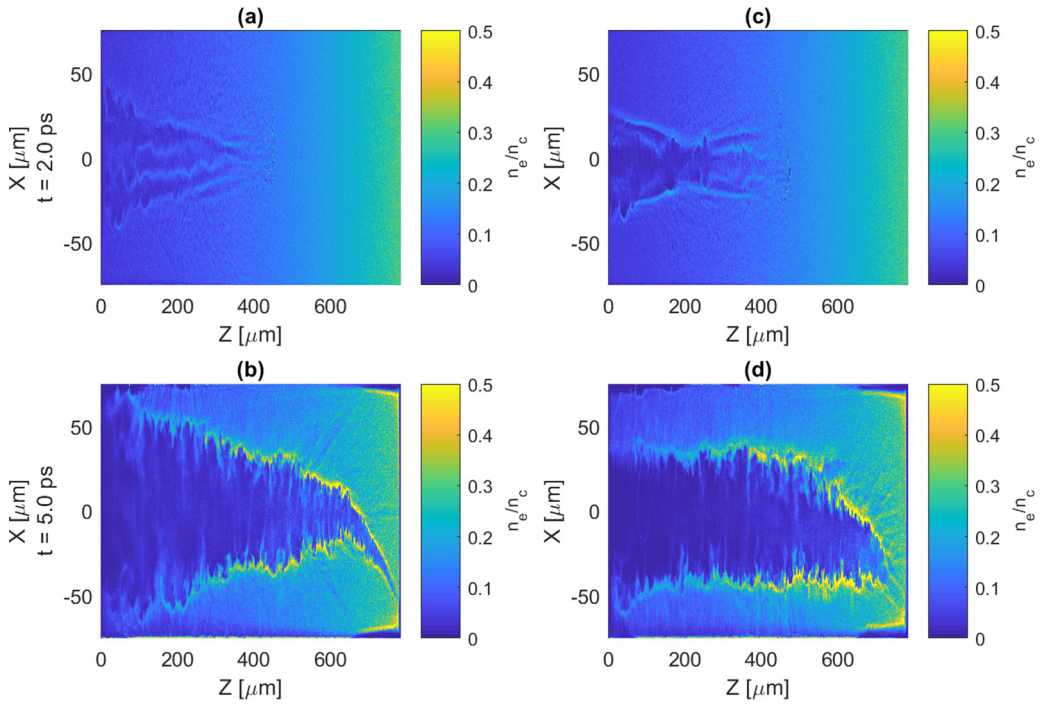

FIG. 10. Simulated channel profiles for a perfect and a speckled beam. Shown are the electron density profiles after [(a) and (c)] 2.5 ps and [(b) and (d)] 5.0 ps for [(a) and (b)] the perfect beam and [(b) and (d)] the imperfect beam.

the self-focusing process. At later times, both simulations' filaments reconnected to form a single channel. However, while the perfect beam did manage to self-focus to a tighter spot, the imperfect beam remained relatively wide.

The original filamentation along the lines of the electromagnetic energy distribution suggests that a successful run which properly simulates the speckling in Fig. 8 would experience more extreme filamentation and therefore supports the hypothesised effects of beam speckling on pulse propagation. Therefore, filamentation in the experimental results can be attributed at least in part to beam speckle. While whole-beam self-focusing was not achieved in this experiment, the results show evidence supporting the scheme for the first time in large-scale-length plasmas by obtaining one of its major purposes—deeper penetration without increased energy requirements.

VII. INTENSITY DEPENDENCE

Perhaps the most interesting result of this experiment comes from the performance of the high-power versus low-power pulses. Previous work has shown that the low-power pulses should require less energy to reach the critical surface than high-power pulses [37]. This result was derived from 2D3V PIC simulations featuring Gaussian pulses propagating through an exponentially increasing plasma with a scale length of 430 μm and various relativistic intensities. Assuming a 1-μm wavelength, pulses with an intensity of 10^{18} W cm^{-2} were expected to reach approximately 0.6 n_c after 100 ps while 10^{19}-W cm^{-2} pulses were predicted to reach approximately 0.4 n_c after 10 ps. This corresponds to an additional 170-μm channel depth for the low-intensity pulses. These parameters are all very similar to those found in this experiment.

An earlier experiment was conducted to confirm these PIC results [43]. The results showed the low-intensity pulses consistently reaching the critical surface while the high-intensity pulses failed to do so, and the channel velocity measurements roughly agreed with Li *et al.*'s predictions. However, that experiment had approximately double the energy in the low-intensity pulses compared to the high-intensity pulses. Thus it is not at all surprising that they would reach a greater overall depth.

Here, where the energy is only 12% greater in the low-power case, a different trend emerges. In the hot plasmas, high-power shots actually outperformed the low-power shots both in terms of channel depth and quality. As can be seen in Fig. 11, the channel itself appears to be narrower and more collimated compared to the low-power case in hot plasmas. This can largely be attributed to the duration of the pulses. A channel's transverse density profile may be approximated by solving [5]:

$$\left(\frac{\partial^2}{\partial t^2} - c_s^2\nabla_\perp^2\right)\frac{n_{i1}}{n_{i0}} \approx \frac{Zm_e}{m_i}c^2\nabla_\perp^2\left(1+\frac{a^2}{2}\right)^{1/2}, \quad (1)$$

where $c_s = (Zk_BT_e/m_i)^{1/2}$ is the sound speed, n_{i0} is the initial density profile, n_{i1} is the perturbation to that initial profile, and the other variables have their traditional assignments. This equation may be integrated assuming 3D cylindrical symmetry and using the two sets of parameters observed in this experiment. Specifically, this means the first integration was through 100 ps using a Gaussian profile for a with a peak value of $a_0 = 0.85$ and 80% of the three-dimensional energy contained in a radius of $r = 18\,\mu$m. The second was through 10 ps with $a_0 = 3.1$ and $r = 15\,\mu$m. Both calculations used Gaussian longitudinal profiles as well. The results are shown in Fig. 12. As can be seen here, the channel walls of the

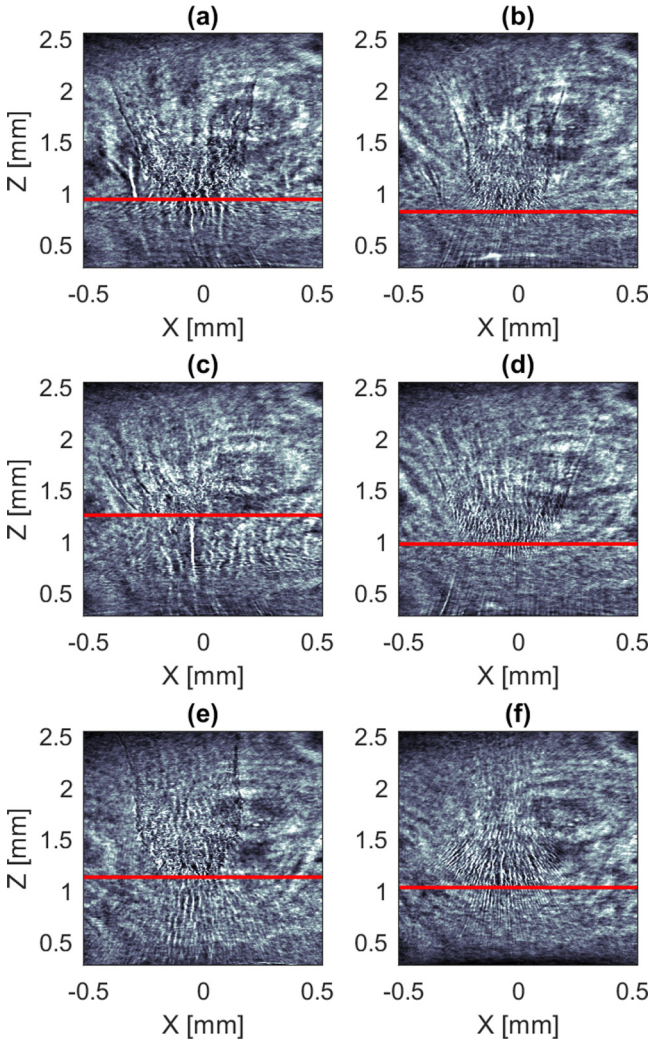

FIG. 11. Shadowgraphy images for the channel depth intensity dependence. Shadowgraphs are shown for the three relevant intensity comparisons. The left column shows the channels formed by the 100-ps pulse while the right column corresponds to the 10-ps pulse. Panels (a) and (b) are in a hot plasma with focal positions at $Z = 0.9$ mm, (c) and(d) are in a hot plasma with focal positions at $Z = 0.3$ mm, and (e) and (f) are in a hot plasma with focal positions at $Z = 1.5$ mm. Superimposed horizontal red lines indicate the measured channel depth. Note that several of these images are reproduced from Figs. 5 and 6 for ease of comparison.

100-ps pulse are much greater than those of the 10-ps pulse and the channel itself is much wider. This matches what is seen in the shadowgraphs as the 100-ps channels are much wider with more distinct walls, corresponding to a greater density gradient.

More importantly and contrary to the above-referenced numerical investigations, in both the hot and cold shots, the high-intensity pulse actually achieved deeper penetration than its low-intensity counterpart despite having less total energy. While more work is required to explain this discrepancy with certainty, evidence suggests that it arises from three-dimensional effects. A follow-up study for the original PIC simulations was performed which featured a single 3D3V PIC simulation [44]. In it, Li *et al.* found that the channel penetrated

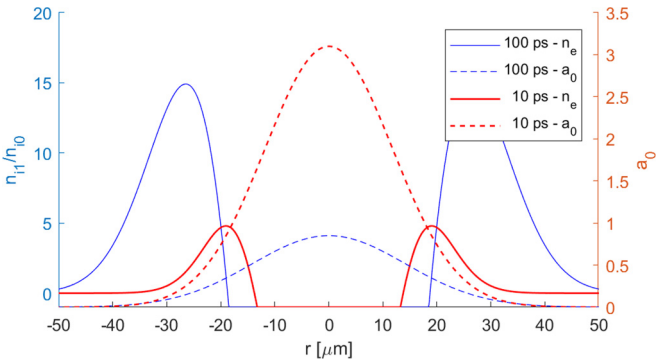

FIG. 12. Integration of channeling profile equation for experiment's pulses. Equation (1) was integrated using the pulse parameters found in this experiment through the end of the pulses' durations.

through the plasma at a much greater velocity and with far fewer chaotic features. The explanation for this is given both by the ease of channel formation in 3D and the focusing of the laser pulse. Each of these points will be analyzed here.

As discussed by Li *et al.* [44], Equation (1) may be integrated using the exact same parameters in both 2D and 3D yet yield lower densities, and thus faster channel formation, in 3D compared to 2D. Mathematically, this is because of the form $\nabla_\perp^2$ takes in each dimension, with $\nabla_{2D}^2 = \partial_r^2$ and $\nabla_{3D}^2 = r^{-1}\partial_r(r\partial_r)$, where cylindrical symmetry has been assumed [44]. Figure 13 shows the result of integrating Equation (1) at various intensities until the 3D channel is fully evacuated on-axis. This corresponds to times $t_1 = 3.758$ ps, $t_3 = 1.732$ ps, and $t_{10} = 0.907$ ps for $a_0 = 1$, $a_0 = 3$, and $a_0 = 10$, respectively. While the channel profile does vary, the density on-axis was the same in 2D at the presented times regardless of intensity. Thus, while dimensionality does affect the channeling speed of pulses, it does so independently of intensity and therefore would not affect the relative performance of the pulses in this experiment.

One important phenomenon missing from Equation (1) and the subsequent analysis is self-focusing. As a pulse continues

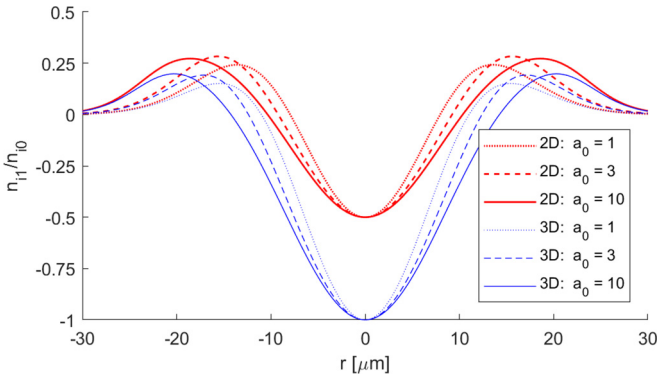

FIG. 13. Integration of channeling profile equation at various intensities. Equation (1) was integrated until the 3D density profile was fully evacuated at various intensities. Red (thick) lines indicate the integration was performed in 2D while blue (thin) lines indicate 3D. Dotted lines correspond to $a_0 = 1$ at $t = 3.758$ ps, dashed lines to $a_0 = 3$ at $t = 1.732$ ps, and solid lines to $a_0 = 10$ at $t = 0.907$ ps.

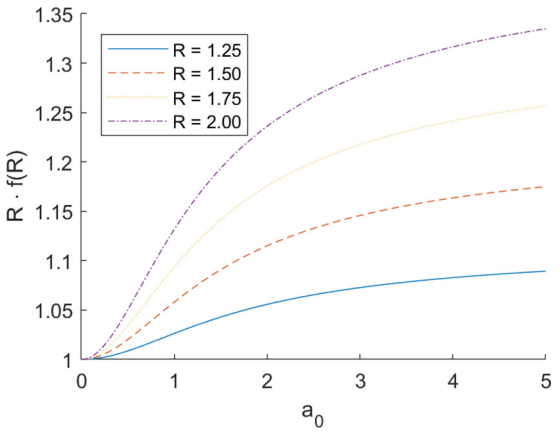

FIG. 14. Channeling velocity dependence on intensity and self-focusing ratio. Plotted is the ratio of channeling velocity when a pulse experiences a self-focusing ratio of R. As can be seen, this has little effect at lower intensities but increases until plateauing at $R^{1/2}$.

to propagate through the plasma, it will ponderomotively and relativistically self-focus. Assuming the laser energy largely stays within the channel, power conservation requires $a^2 w = a_0^2 w_0$ in 2D and $a^2 w^2 = a_0^2 w_0^2$ in 3D where w is the channel width and 0 subscripts indicate vacuum values [44]. Thus, the intensity will increase by a factor of the self-focusing ratio, $R \equiv w_0/w > 1$, in 3D compared to 2D. According to the physical models present in the literature, the hole-boring depth is given by [32,45]:

$$d_{\mathrm{hb}} = a_0 c\tau \left(\frac{n_c}{2n_e} \frac{Z m_e}{m_i} \right)^{1/2}, \tag{2}$$

while the channeling depth is given by [32,46]:

$$d_{\mathrm{ch}} = \frac{a_0^2}{\gamma - 1} \frac{n_c}{2\bar{n}_e} c\tau. \tag{3}$$

Thus, comparing 3D to 2D, self-focusing will increase the depth achieved in the hole-boring regime by a factor of $R^{1/2}$ while the channeling depth will be increased by $Rf(R)$, where $f(R) \equiv [\gamma(R) - 1)/(\gamma(R^2) - 1]$ and $\gamma(\xi) = (1 + \xi a_0^2/2)^{1/2}$ is the Lorentz factor for a linear pulse. The increase to the channeling depth therefore approaches $R^{1/2}$ as a_0 increases, but it has a strong intensity dependence for smaller values of a_0.

Figure 14 plots $Rf(R)$ as a function of a_0 to illustrate this intensity dependence. As can be seen here, the channeling depth experiences little effect from self-focusing for low intensities. This is in line with expectations as the low-intensity approximation of the channeling depth is independent of intensity. However, this function begins to increase rapidly with a_0 until plateauing at $R^{1/2}$. As a result, the high-intensity pulses in this experiment would have experienced greater penetration while still in the channeling regime than the low-intensity pulses. This could then alter the relative channel depths seen within the experiment.

In order to properly verify these effects, several three-dimensional PIC simulations would be required to recreate the original simulations performed by Li *et al.* [37]. Unfortunately, this is currently computationally infeasible. Instead, a series of 2D cylindrical simulations have been designed to approximate the three-dimensional behavior of a pulse. OSIRIS currently only has limited support for such simulations, though this is expected to be rectified in the future.

VIII. LEADING FILAMENTS

As stated earlier, the minor filament-like structures in front of the channel were not included in the calculation of the channel depths. Examples of these filaments are shown in Fig. 15. As this figure illustrates, these filaments took various forms but were nonetheless present in some manner in each shot. Figure 15(a) shows faint, straight perturbations, while Fig. 15(b)'s front filaments are much more pronounced. Figure 15(c) appears to be some form of a combination between the two. All of these features are extremely narrow, between 3 and 5 μm wide, and often extend beyond the critical surface, suggesting that they are formed by fast electrons rather than the channeling pulse directly. More specifically, the faint filaments are caused by the bunching of fast electrons as they propagate

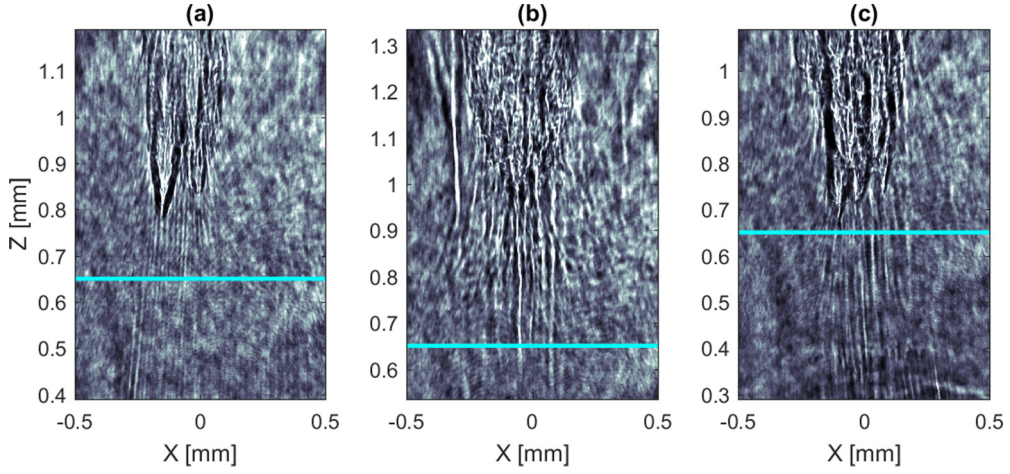

FIG. 15. Examples of leading filaments. Cropped shadowgraphs are shown for (a) 10-ps pulse at half energy, focused at $Z = 1.5$ mm, (b) 100-ps pulse focused at $Z = 0.9$ mm, and (c) 100-ps pulse focused at $Z = 1.5$ mm. Superimposed horizontal cyan lines indicate the critical surface based on the AFR reconstruction.

through the plasma, consistent in structure with previous experiments and simulations [47–49]. The more intensely focused filaments are caused by electron beams which have been pinched together by the strong magnetic fields within the channels—a phenomenon first observed by Pukhov and Meyer-ter-Vehn in 1996 using PIC simulations [50].

While separately these structures are interesting for the study of electron transport, they were not included in the channel depth calculations for a variety of reasons. Their formation was not predictable within this experiment, and thus they are not reliable quantifiers when determining the depth a channeling pulse may achieve. Further, Sec. VII compares the channel depths to those predicted by Ref. [37]. That paper defined the channel depth as the location where the averaged density fell below 10% of the critical density. This averaging was reportedly done over the plasma within a 7.5-μm radius of the propagation axis. As such, these structures would have been too narrow to have affected the calculation in this previously published work, and including them here would make for an inappropriate comparison.

IX. SECONDARY DIAGNOSTICS

The secondary diagnostics showed strong agreement with the trends discussed above. Fast electrons will be generated through the channeling process, and these will generally diverge at angles up to 55° [23,51,52]. Thus, the deeper the channel, the more concentrated these fast electrons will be as they reach the rear of the copper-backed target. This in turn will raise the number of electrons collisionally ejected from lower shells in the copper atoms, and the K_α signal seen in the von Hamos spectrometer will increase. Further, the cross section of K_α florescence varies slowly with electron energy [53–55]. Therefore, while this diagnostic is not suitable for comparing high-intensity to low-intensity shots, it does adequately capture the relative fast electron flux when varying the focal position for each intensity.

Figure 16(a) shows an example image plate scan from the von Hamos spectrometer. The signal has two peaks with the larger in amplitude corresponding to Cu K_α and the lower to Cu K_β. Each image was integrated vertically to give a total spectrum and is plotted as a function of energy in Fig. 16(b). The total Cu K_α yield was found by integrating the signal within 150 eV of the 8048-eV peak, indicated by dashed lines superimposed on the first two images of this figure. This integration was performed twice more with a radius 25% larger and 25% smaller about the K_α peak to provide error measurements of this calculation. The background was calculated through linear interpolation between these endpoints. The resulting yield is plotted as a function of focal density in Fig. 16(c). Notice that this yield closely follows the trends in channel depth shown in Fig. 4. The shots which produced the deepest channels also had the brightest K_α yields. This is as expected and provides support to the depth measurements as a function of focal position.

One additional diagnostic worth discussing in this experiment is polarimetry using the 4ω probe. After the probe beam passes through the interaction region, it is split by a Wollaston prism, creating a P image and an S image and captured by a charge-coupled device (CCD) camera. These images

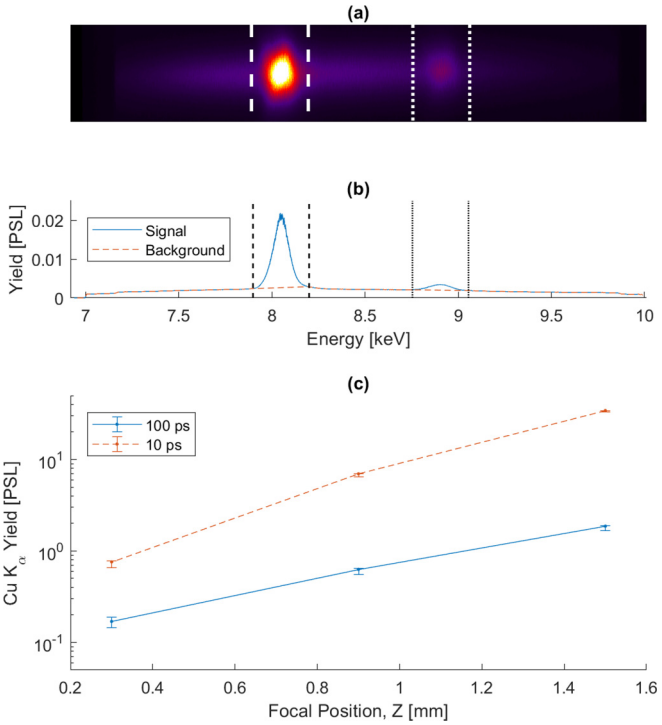

FIG. 16. Von Hamos spectrometer output and Cu K_α yield. An example von Hamos spectrometer signal is shown in (a) with white dashed lines indicating the Cu K_α region and dotted lines indicating the Cu K_β region. An integrated lineout is shown in (b) along with the background profile. The K_α region was then integrated within a 0.15-keV range of its peak to calculate the total Cu K_α yield plotted in (c) for each hot plasma shot.

correspond to the two orthogonal polarizations defined by the prism's rotation angle. A script was written to identify the two images within the detector's output using a k-means clustering algorithm. These images were then aligned using Matlab's built-in image registration scripts, and the polarization rotation angle was calculated [56]. There was difficulty with the polarimetry beam's transport, likely due to misalignment of the Wollaston prism and lens imprinting. As a result, the detectors were not evenly illuminated even with no plasma present, and the signals experienced bubblelike distortions. These distortions may be seen in Fig. 17(a). It is also clear from this figure that the P image, boxed in dashed lines, was significantly brighter than the S image, boxed in solid lines. As a result, when calculating the probe's polarization rotation angle, there was an offset towards positive values as is evident in Fig. 17(b). In order to compensate for the illumination differences, the signal images were normalized using data from the shots without any plasma. The results, shown in Fig. 17(c) had poor signal-to-noise ratios, and thus the magneti fields were not able to be quantitatively measured. Note that the large specks in Figs. 17(b) and 17(c) are due to dust on the detector.

Despite the implementation issues with this diagnostic, one interesting trend is discernible. Each filament of a channel will create its own left-hand azimuthal magnetic fields. These fields are formed by the strong current generated as electrons are accelerated forward by the ponderomotive force along the channel's axis and by the return currents along the channel's

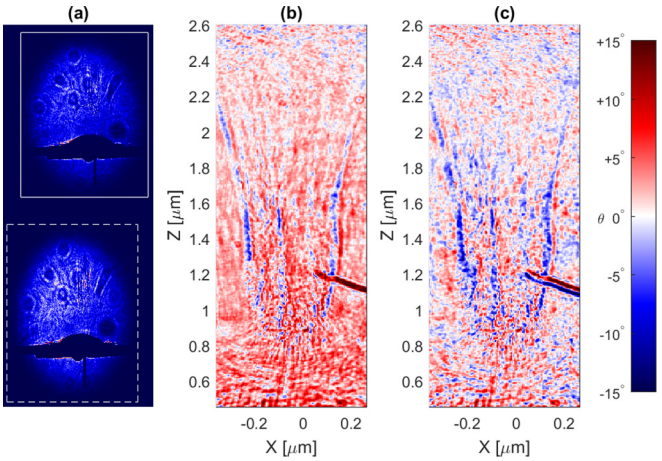

FIG. 17. Polarimetry of the channels. The raw signal for the 10-ps pulse focused at $Z = 0.9$ mm is shown in (a). Superimposed white boxes indicate the S (solid lines) and P (dashed lines) images. Panel (b) shows the cropped calculation of the beam rotation angle, θ without any normalizations. Panel (c) shows the same calculation after normalizing the S and P images using the plasma-free shot's images. The axes on (b) and (c) are not exact due to the image transformations involved in aligning the two raw images but are well matched to the shadowgraphy results and therefore provide a reasonable estimate.

walls. These fields continue to persist beyond the end of the channeling pulse as electron vortices form [4,57,58]. As such, this diagnostic is well suited for identifying filamentation within this experiment. While the noise was too large to quantitatively determine the magnetic fields, there are clear striations along the channel's path. These support the conclusion that filamentation was present and caused the channel to appear wider than the vacuum focal spots would have suggested.

X. CONCLUSIONS

The results of an OMEGA EP experiment designed to determine the optimum channeling parameters in an inhomogeneous plasma have been presented. The final density profile and channel formation was observed using a high-frequency transverse probe. The results showed that minimizing the delay between drive and channeling pulses is crucial for the formation of a controlled channel and maximizing its penetration into the plasma. Additionally, the channels deepened as pulses were focused at lower densities in the unperturbed plasma. Both of these results were consistent with previous experiments and the superpenetration (whole-beam self-focusing) schemes present in the literature.

Interestingly, the 10-ps pulses consistently reached a deeper depth than their 100-ps counterparts despite only having approximately 90% of the longer pulses' energy. This is in contrast to previous predictions and may be the result of three-dimensional effects such as increased channel formation speed and ponderomotive pressures. While more work is required in order to confirm this as the root cause, it does highlight the need to include three-dimensional effects into experimental designs and numerical simulations.

ACKNOWLEDGMENTS

This material is based on work supported by the Department of Energy National Nuclear Security Administration under Award No. DE-NA0001944, the Laboratory Basic Science Program, the University of Rochester, and the New York State Energy Research and Development Authority. The authors would also like to acknowledge DOE Grant NO. DE-SC0014666 for the support of this work. The FLASH code used in this work was developed in part by the DOE NNSA ASC- and DOE Office of Science ASCR-supported Flash Center for Computational Science at the University of Chicago. The support of DOE does not constitute an endorsement by DOE of the views expressed in this article. Part of the research has been supported by JSPS-S class fund (15H05751-70171741). The authors thank the OSIRIS consortium for the use of OSIRIS. We would also like to thank the ARCHER UK National Supercomputing Service. This work has further been carried out within the framework of the EUROfusion Consortium and has received funding from the Euratom research and training programme 2014-2018 under Grant No. 633053. The views and opinions expressed herein do not necessarily reflect those of the European Commission. The authors further acknowledge the support of the Plasma HEC Consortium, EPSRC Grant No. EP/L00023711.

[1] W. B. Mori, IEEE J. Quantum Electron. **33**, 1942 (1997).
[2] F. Cattani, A. Kim, D. Anderson, and M. Lisak, Phys. Rev. E **64**, 016412 (2001).
[3] A. Kim, M. Tushentsov, F. Cattani, D. Anderson, and M. Lisak, Phys. Rev. E **65**, 036416 (2002).
[4] L. Willingale, P. M. Nilson, A. G. R. Thomas, J. Cobble, R. S. Craxton, A. Maksimchuk, P. A. Norreys, T. C. Sangster, R. H. H. Scott, C. Stoeckl, C. Zulick, and K. Krushelnick, Phys. Rev. Lett. **106**, 105002 (2011).
[5] K. Krushelnick, A. Ting, C. I. Moore, H. R. Burris, E. Esarey, P. Sprangle, and M. Baine, Phys. Rev. Lett. **78**, 4047 (1997).
[6] G. Sarri, D. K. Singh, J. R. Davies, F. Fiuza, K. L. Lancaster, E. L. Clark, S. Hassan, J. Jiang, N. Kageiwa, N. Lopes, A. Rehman, C. Russo, R. H. H. Scott, T. Tanimoto, Z. Najmudin, K. A. Tanaka, M. Tatarakis, M. Borghesi, and P. A. Norreys, Phys. Rev. Lett. **105**, 175007 (2010).
[7] M. Borghesi, A. J. MacKinnon, L. Barringer, R. Gaillard, L. A. Gizzi, C. Meyer, O. Willi, A. Pukhov, and J. Meyer-ter-Vehn, Phys. Rev. Lett. **78**, 879 (1997).
[8] H. Habara, K. L. Lancaster, S. Karsch, C. D. Murphy, P. A. Norreys, R. G. Evans, M. Borghesi, L. Romagnani, M. Zepf, T. Norimatsu, Y. Toyama, R. Kodama, J. A. King, R. Snavely, K. Akli, B. Zhang, R. Freeman, S. Hatchett, A. J. MacKinnon, P. Patel, M. H. Key, C. Stoeckl, R. B. Stephens, R. A. Fonseca, and L. O. Silva, Phys. Rev. E **70**, 046414 (2004).
[9] N. Naumova, T. Schlegel, V. T. Tikhonchuk, C. Labaune, I. V. Sokolov, and G. Mourou, Phys. Rev. Lett. **102**, 025002 (2009).

[10] A. P. L. Robinson, Phys. Plasmas **18**, 056701 (2011).
[11] A. P. L. Robinson, R. M. G. M. Trines, N. P. Dover, and Z. Najmudin, Plasma Phys. Controlled Fusion **54**, 115001 (2012).
[12] I. V. Pogorelsky *et al.*, Ion acceleration by laser hole-boring into plasmas, in *Advanced Accelerator Concepts: 15th Advanced Accelerator Concepts Workshop*, AIP Conf. Proc. No. 1507 (AIP, New York, 2013), pp. 814–819.
[13] D. Wu *et al.*, Phys. Plasmas **20**, 023102 (2013).
[14] S. M. Weng *et al.*, Phys. Plasmas **21**, 012705 (2014).
[15] J. Faure *et al.*, Nature **444**, 737 (2006).
[16] W. P. Leemans *et al.*, Nat. Phys. **2**, 696 (2006).
[17] K. Nakamura *et al.*, Phys. Plasmas **14**, 056708 (2007).
[18] T. Matsuoka *et al.*, Plasma Phys. Controlled Fusion **51**, 095003 (2009).
[19] E. N. Nerush and I. Y. Kostyukov, Plasma Phys. Controlled Fusion **57**, 035007 (2015).
[20] S. Kneip, S. R. Nagel, C. Bellei, N. Bourgeois, A. E. Dangor, A. Gopal, R. Heathcote, S. P. D. Mangles, J. R. Marquès, A. Maksimchuk, P. M. Nilson, K. T. Phuoc, S. Reed, M. Tzoufras, F. S. Tsung, L. Willingale, W. B. Mori, A. Rousse, K. Krushelnick, and Z. Najmudin, Phys. Rev. Lett. **100**, 105006 (2008).
[21] M. Tabak *et al.*, Phys. Plasmas **1**, 1626 (1994).
[22] R. S. Craxton *et al.*, Phys. Plasmas **22**, 110501 (2015).
[23] A. J. Kemp *et al.*, Nucl. Fusion **54**, 054002 (2014).
[24] M. Tabak, P. A. Norreys, V. T. Tikhonchuk, and K. A. Tanaka, Nucl. Fusion **54**, 054001 (2014).
[25] E. M. Epperlein, Phys. Rev. Lett. **65**, 2145 (1990).
[26] R. Bingham, R. Short, E. Williams, D. Villeneuve, and M. C. Richardson, Plasma Phys. Controlled Fusion **26**, 1077 (1984).
[27] E. Higson *et al.*, New J. Phys. **15**, 015027 (2013).
[28] C. E. Max, J. Arons, and A. B. Langdon, Phys. Rev. Lett. **33**, 209 (1974).
[29] P. Kaw, Phys. Fluids **16**, 1522 (1973).
[30] Z. Najmudin *et al.*, Phys. Plasmas **10**, 438 (2003).
[31] L. M. Chen *et al.*, Phys. Plasmas **14**, 040703 (2007).
[32] L. Ceurvorst *et al.*, New J. Phys. **18**, 053023 (2016).
[33] K. A. Tanaka *et al.*, Phys. Plasmas **7**, 2014 (2000).
[34] T. Matsuoka *et al.*, Plasma Phys. Controlled Fusion **50**, 105011 (2008).
[35] A. L. Lei *et al.*, Phys. Plasmas **16**, 056307 (2009).
[36] S. Palaniyappan *et al.*, Nat. Phys. **8**, 763 (2012).
[37] G. Li, R. Yan, C. Ren, T.-L. Wang, J. Tonge, and W. B. Mori, Phys. Rev. Lett. **100**, 125002 (2008).
[38] D. Haberberger *et al.*, Phys. Plasmas **21**, 056304 (2014).
[39] L. Willingale *et al.*, J. Phys.: Conf. Ser. **688**, 012126 (2016).
[40] S. Ivancic, Channeling experiments on OMEGA, Ph.D. thesis, University of Rochester, 2015.
[41] R. A. Fonseca *et al.*, OSIRIS: A three-dimensional, fully relativistic particle in cell code for modeling plasma based accelerators, in *Proceedings of Computational Science-ICCS, Pt III*, Lecture Notes in Computer Science Vol. 2331 (Springer, Berlin, 2002), pp. 342–351.
[42] ARCHER UK National Supercomputing Services, http://www.archer.ac.uk.
[43] S. Ivancic, D. Haberberger, H. Habara, T. Iwawaki, K. S. Anderson, R. S. Craxton, D. H. Froula, D. D. Meyerhofer, C. Stoeckl, K. A. Tanaka, and W. Theobald, Phys. Rev. E **91**, 051101(R) (2015).
[44] G. Li, R. Yan, C. Ren, J. Tonge, and W. B. Mori, Phys. Plasmas **18**, 042703 (2011).
[45] S. C. Wilks, W. L. Kruer, M. Tabak, and A. B. Langdon, Phys. Rev. Lett. **69**, 1383 (1992).
[46] L. Willingale, S. R. Nagel, A. G. R. Thomas, C. Bellei, R. J. Clarke, A. E. Dangor, R. Heathcote, M. C. Kaluza, C. Kamperidis, S. Kneip, K. Krushelnick, N. Lopes, S. P. D. Mangles, W. Nazarov, P. M. Nilson, and Z. Najmudin, Phys. Rev. Lett. **102**, 125002 (2009).
[47] B. Cohen, A. J. Kemp, and L. Divol, J. Comput. Phys. **229**, 4591 (2010).
[48] S. Chawla, M. S. Wei, R. Mishra, K. U. Akli, C. D. Chen, H. S. McLean, A. Morace, P. K. Patel, H. Sawada, Y. Sentoku, R. B. Stephens, and F. N. Beg, Phys. Rev. Lett. **110**, 025001 (2013).
[49] L. Gremillet, G. Bonnaud, and F. Amiranoff, Phys. Plasmas **9**, 941 (2002).
[50] A. Pukhov and J. Meyer-ter-Vehn, Phys. Rev. Lett. **76**, 3975 (1996).
[51] R. H. H. Scott *et al.*, Phys. Plasmas **19**, 053104 (2012).
[52] L. Volpe, J.-L. Feugeas, P. Nicolai, J. J. Santos, M. Touati, J. Breil, D. Batani, and V. Tikhonchuk, Phys. Rev. E **90**, 063108 (2014).
[53] C. Hombourger, J. Phys. B: Atomic **31**, 3693 (1998).
[54] C. Reich, P. Gibbon, I. Uschmann, and E. Förster, Phys. Rev. Lett. **84**, 4846 (2000).
[55] J. P. Santos, F. Parente, and Y.-K. Kim, J. Phys. B **36**, 4211 (2003).
[56] F. F. Chen, *Introduction to Plasma Physics and Controlled Fusion*, 2nd. ed. (Springer, Boston, MA, 1984).
[57] M. Tatarakis, J. R. Davies, P. Lee, P. A. Norreys, N. G. Kassapakis, F. N. Beg, A. R. Bell, M. G. Haines, and A. E. Dangor, Phys. Rev. Lett. **81**, 999 (1998).
[58] Y. Uematsu *et al.*, Rev. Sci. Instrum. **85**, 11E612 (2014).